Non-Lumped Microwave Topolectrical Resonator Based on the Su–Schrieffer–Heeger Model

Chengxin Yu[1,2] and Xiao Zhang[1,2*]

[1]*School of Physics, Sun Yat-sen University, Guangzhou 510275, China*
[2]*Guangdong Provincial Key Laboratory of Magnetoelectric Physics and Devices, School of Physics, Sun Yat-sen University, Guangzhou 510275, China*

(Received 31 March 2025; accepted manuscript online 21 May 2025)

Topological states realized in metamaterials have provided a versatile platform for exploring topological physics and enabling novel applications, with topolectrical circuits emerging as a prominent example. However, previous research in this field has primarily focused on lumped-element implementations, while non-lumped microwave circuits remain relatively underexplored. In this work, we design and investigate a one-dimensional non-lumped Su–Schrieffer–Heeger topolectrical circuit composed of copper parallel-plate transmission lines and inductors, offering compatibility with integrated microwave applications. Full-wave microwave simulations in the 0–10 GHz range show excellent agreement with theoretical predictions. The impedance spectrum of a five-unit-cell system displays periodic resonant passbands and stopbands corresponding to bulk states, while distinct high-Q (on the order of 10^2) topological boundary resonances (TBRs) emerge within the stopbands, indicating the presence of localized edge states. Furthermore, the TBRs vanish when the system is reconfigured into the trivial phase, providing direct evidence of its topological nature. These response characteristics make the proposed resonator a promising candidate for future microwave devices and topological circuit applications.

DOI: 10.1088/0256-307X/42/7/070704 CSTR: 32039.14.0256-307X.42.7.070704

1. Introduction. Topolectrical circuits, which realize coupling between lattice sites through discrete electronic components, offer unprecedented control over individual coupling parameters.[1] Since the initial demonstrations of two-dimensional LC networks emulating the Hofstadter model[2] and the non-Abelian Aharonov–Bohm effect[3] in 2015, research on topolectrical circuits has progressed rapidly, owing to the platform's unique advantages and application potential.

Today, this field encompasses a wide variety of topological systems characterized by distinct nontrivial invariants, including winding numbers,[1,4–14] Chern numbers,[1,12,15–19] and knot invariants.[20–22] These realizations span dimensionalities from one to beyond three dimensions.[1–20,23–43]

However, the aforementioned studies primarily focus on the measurement of electrical quantities in lumped-element circuits. In non-lumped regimes, where component dimensions are comparable to the operating wavelength, it becomes essential to consider the wave nature of electromagnetic fields. The realization of topological states under such conditions has largely relied on optical platforms, such as optical waveguides,[44–59] while the exploration of non-lumped topolectrical circuits remains relatively limited.

In existing studies that attempt to realize topological states in non-lumped electrical systems,[60–66] transmission lines have been employed as distributed parameter elements, demonstrating notable scientific interest and application potential. Nevertheless, several critical aspects remain insufficiently addressed, including the incorporation of the Laplacian formalism,[1] the treatment of realistic lossy transmission lines, and the systematic characterization of measurable electrical quantities. Our work aims to bridge these gaps and provide a comprehensive framework for non-lumped topolectrical systems.

In this study, we present a non-lumped circuit implementation of the one-dimensional Su–Schrieffer–Heeger (SSH) model,[67] which has been extensively utilized in lumped-element topolectrical circuits,[1,4,5,8,23–29,34] one-dimensional photonic crystals,[44–47] and optical waveguide systems.[52–54,56,57] In contrast to the coaxial cable approach proposed by Whittaker *et al.*,[65,66] our design employs parallel-plate transmission lines and lumped inductors to construct a topolectrical circuit optimized for integrated, low-impedance, and high-power microwave resonators.

The circuit utilizes copper conductors, with air and Al_2O_3 ceramic as dielectric materials. High-frequency electromagnetic simulations were performed to account for realistic lossy conditions. In a system comprising only five unit cells, the input impedance reveals two distinct topological boundary resonance (TBR) peaks, located at approximately 3.47 GHz and 7.97 GHz, with high quality factors (Q) of 188.75 and 279.95, respectively. Under topologically nontrivial conditions, the voltage amplitudes at odd-numbered ports decay exponentially along the circuit at the TBR frequencies, while showing oscillatory behav-

*Corresponding author. Email: zhangxiao@mail.sysu.edu.cn
© 2025 Chinese Physical Society and IOP Publishing Ltd. All rights, including for text and data mining, AI training, and similar technologies, are reserved.

ior at bulk resonance frequencies. This contrast provides a clear method for distinguishing topological boundary states from bulk states.

Moreover, the TBR peak positions can be tuned by adjusting the transmission line lengths, offering tunability across a broad frequency range and thereby enhancing the circuit's potential for practical microwave applications. [68,69]

2. Circuit Design and Laplacian Matrix. The non-lumped nature of transmission line elements necessitates the use of a distributed-parameter model. As illustrated in Fig. 1(a), an infinitesimal segment of a transmission line of length Δz can be modeled as a two-port network characterized by a series resistance R_0 and inductance L_0 per unit length, as well as a shunt conductance G_0 and capacitance C_0 per unit length between the conductors.

Accordingly, the transmission matrix of a finite-length transmission line segment of length l_j (for $j = 1, 2$) is given by [70]

$$\boldsymbol{T}_j = \begin{bmatrix} A_j & B_j \\ C_j & D_j \end{bmatrix} = \begin{bmatrix} \cosh(\gamma_j l_j) & Z_{0,j}\sinh(\gamma_j l_j) \\ \frac{\sinh(\gamma_j l_j)}{Z_{0,j}} & \cosh(\gamma_j l_j) \end{bmatrix}, \tag{1}$$

which describes the voltage and current relationship between the two ports of the transmission line.

For high-frequency sinusoidal steady-state signals, i.e., when $R_0 \ll \omega L_0$ and $G_0 \ll \omega C_0$, the characteristic impedance Z_0 and the complex propagation constant γ can be approximated under the low-loss condition [71] as

$$\gamma = \frac{1}{2}\left(R_0\sqrt{\frac{C_0}{L_0}} + G_0\sqrt{\frac{L_0}{C_0}}\right) + \mathrm{i}\omega\sqrt{L_0 C_0},$$
$$Z_0 = \sqrt{\frac{L_0}{C_0}}. \tag{2}$$

We construct a non-lumped transmission-line SSH topolectrical circuit by arranging alternating cascades of two types of transmission lines, labeled as line 1 and line 2 [marked in red and blue in Fig. 1(b)], forming a one-dimensional chain. Identical inductors L are connected in shunt between adjacent transmission lines at the ports, as illustrated in Fig. 1(b). Structurally, the nodes labeled $1, 2, \ldots, 2N$, where inductors are placed, correspond to atomic sites in the SSH model, with transmission lines 1 and 2 representing intracell hopping amplitude v and intercell hopping amplitude w, respectively.

In this design, the smallest repeating structural unit consists of two transmission lines and two inductors [see Fig. 1(c)], which directly maps to a unit cell in the SSH model.

Furthermore, when performing frequency-domain nodal analysis on the circuit, the network can be represented as an undirected graph, where the Laplacian matrix $\boldsymbol{L}$ relates the node current source vector $\boldsymbol{I}$ to the node voltage vector $\boldsymbol{V}$ via the relation $\boldsymbol{I} = \boldsymbol{L}\boldsymbol{V}$. This formulation is formally analogous to the stationary Schrödinger equation $\boldsymbol{H}\boldsymbol{\psi} = E\boldsymbol{\psi}$. In our system, the $2N$ port voltages constitute the vector $\boldsymbol{V}$, while the vector $\boldsymbol{I}$ corresponds to the algebraic sum of currents leaving each node.

The transmission relationship between voltages and currents at adjacent nodes is governed by Eq. (1). By applying the port network parameter conversion method [72] to Eq. (1) and enforcing Kirchhoff's current law at each node, we derive the Laplacian matrix for the entire one-dimensional non-lumped topolectrical circuit [a detailed derivation is provided in the Supplementary Materials (SM)],

$$\boldsymbol{L} = \begin{bmatrix} Y_s & -\frac{1}{B_1} & 0 & 0 & \cdots & 0 & 0 \\ -\frac{1}{B_1} & Y_s & -\frac{1}{B_2} & 0 & \cdots & 0 & 0 \\ 0 & -\frac{1}{B_2} & Y_s & -\frac{1}{B_1} & \cdots & 0 & 0 \\ 0 & 0 & -\frac{1}{B_1} & Y_s & \cdots & 0 & 0 \\ \vdots & \vdots & \vdots & \vdots & \ddots & \vdots & \vdots \\ 0 & 0 & 0 & 0 & \cdots & Y_s & -\frac{1}{B_1} \\ 0 & 0 & 0 & 0 & \cdots & -\frac{1}{B_1} & Y_s \end{bmatrix}, \tag{3}$$

in which the port self-admittance is defined as

$$Y_s = \frac{A_1}{B_1} + \frac{A_2}{B_2} + \frac{1}{\mathrm{i}\omega L}, \tag{4}$$

where A_1, B_1, A_2, and B_2 are parameters derived from Eq. (1).

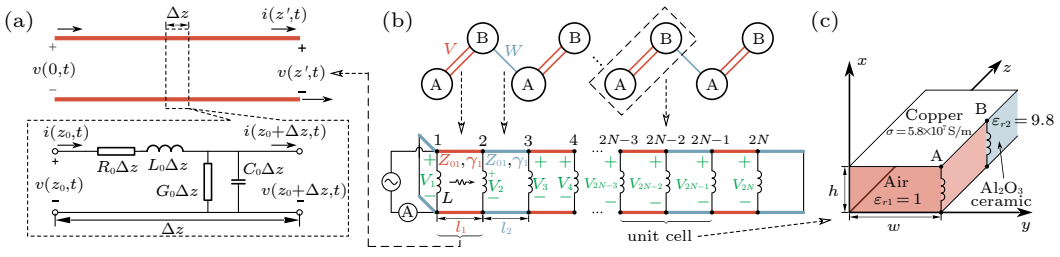

Fig. 1. Schematic diagram of the construction process for a one-dimensional non-lumped transmission line topolectrical circuit. (a) Distributed-parameter model of transmission line 1 (red), characterized by four equivalent lumped parameters, R_0, L_0, G_0, and C_0, over an infinitesimal segment Δz. This model is equally applicable to transmission line 2 (blue). (b) A non-lumped circuit for simulating the SSH model. The upper portion of the figure depicts the SSH model in an electronic system, while the lower portion presents a schematic of the corresponding non-lumped circuit. The red and blue bold lines represent two types of transmission lines. They are arranged in an alternating pattern, and the inductors at all ports exhibit identical inductance values. To ensure that every node in the circuit system has the same degree (two connections from the transmission line network plus one branch from the inductor), we connected a transmission line network 2 with one end short-circuited in parallel at ports 1 and $2N$. (c) A circuit unit cell composed of an inductor and two distinct copper parallel-plate transmission lines (with dielectric materials of air and Al_2O_3 ceramic, respectively).

3. Numerical Calculation and Simulation. In prior studies on non-lumped topolectrical circuits,[62–66] coaxial cables have been widely adopted due to their broad bandwidth and ease of use. However, their cylindrical geometry poses challenges for integration with active components in planar circuits. In contrast, we employ a more integration-friendly parallel-plate transmission line structure and perform high-frequency electromagnetic simulations using Ansys HFSS. The simulation results show good agreement with the theoretical calculations.

As shown in Fig. 1(c), the designed structure confines voltage and current between two parallel conducting plates (with conductivity σ), separated by a dielectric layer characterized by complex permittivity $\epsilon = \epsilon' - \mathrm{i}\epsilon''$ and permeability μ. The electromagnetic field propagates in the transverse electromagnetic mode. Let w and h denote the width and height of the transmission line cross-section, respectively. The distributed circuit parameters used in Eq. (2) are then given by[71]

$$\begin{aligned} R_0 &= \frac{1}{w}\sqrt{\frac{2\omega\mu}{\sigma}}\,, & G_0 &= \omega\epsilon''\frac{w}{h}\,, \\ L_0 &= \mu\frac{h}{w}\,, & C_0 &= \epsilon'\frac{w}{h}\,. \end{aligned} \tag{5}$$

In the actual implementation of our circuit system, the parallel-plate conductors are made of copper ($\sigma = 5.8 \times 10^7\,\mathrm{S/m}$). The dielectric materials used for transmission line 1 and line 2 are air and Al_2O_3 ceramic (with relative permittivity $\epsilon_\mathrm{r} = 9.8$), respectively. A 0.1 nH lumped inductor is inserted at the interface between dielectric segments.

To minimize fringe effect, the dielectric layer is designed with a width of $w = 30\,\mathrm{mm}$, significantly larger than its height $h = 0.5\,\mathrm{mm}$, resulting in a ratio of $w = 60h$ with only 2.92% deviation in Z_{01} between HFSS simulation and theoretical calculations. Based on these structural parameters and applying Eqs. (2) and (5), the transmission characteristics of line 1 and line 2 can be expressed as follows:

$$\begin{aligned} &\gamma_1(\omega) = 5.53\times10^{-7}\sqrt{\omega} + \mathrm{i}\,3.34\times10^{-9}\omega \quad [\mathrm{m}^{-1}], \\ &\gamma_2(\omega) = 1.73\times10^{-6}\sqrt{\omega} + \mathrm{i}\,1.04\times10^{-8}\omega \quad [\mathrm{m}^{-1}], \\ &Z_{01} = 6.28\ \Omega, \quad Z_{02} = 2.01\ \Omega. \end{aligned} \tag{6}$$

In the microwave frequency range (300 MHz–300 GHz), the real part of γ, which accounts for losses due to R_0 and G_0, can be treated as a small perturbation compared to its imaginary part. Under this approximation, and by combining Eqs. (1) and (6), the topological phase transition parameter t for the one-dimensional non-lumped transmission-line circuit can be approximated as

$$t = \frac{-1/B_1}{-1/B_2} \approx \frac{0.32\sin(1.04\times10^{-8}\omega l_2)}{\sin(3.34\times10^{-9}\omega l_1)}, \tag{7}$$

which is derived from Eq. (3). A detailed derivation is provided in the SM.

For a five-unit-cell system operating at a selected microwave frequency (e.g., 1 GHz), varying the relative lengths of transmission line segments 1 and 2 modulates the system's Laplacian eigenvalue spectrum, as shown in Figs. 2(a) and 2(b). The yellow spectral lines correspond to topological boundary states localized at ports 1 and $2N$. As the ratio l_2/l_1 increases continuously from zero, the bandgap between the green eigenvalue clusters, representing bulk states, first closes and then reopens. This bandgap closure and reopening signify a topological phase transition, analogous to the transition between nontrivial and trivial phases in quantum SSH models.

We now proceed to analyze the system's frequency response characteristics. In our design, the unit cell illustrated in Fig. 1(c) is periodically repeated. According to microwave filter theory,[71] such a periodic structure exhibits a fundamental passband-stopband behavior. In the limit where the number of unit cells $N \to \infty$, the passband can be determined from the transmission matrix of a single unit cell, under periodic boundary conditions (PBC).

Specifically, the overall transmission matrix of a unit cell is given by

$$\boldsymbol{T}_0 = \boldsymbol{T}_L\boldsymbol{T}_1\boldsymbol{T}_L\boldsymbol{T}_2 = \begin{bmatrix} A_0 & B_0 \\ C_0 & D_0 \end{bmatrix}, \tag{8}$$

where the shunt inductor matrix is

$$\boldsymbol{T}_L = \begin{bmatrix} 1 & 0 \\ (\mathrm{i}\omega L)^{-1} & 1 \end{bmatrix}, \tag{9}$$

and $\boldsymbol{T}_{1,2}$ are the transmission matrices of the respective transmission lines as defined in Eq. (1).

The passband of the infinitely long circuit chain corresponds to those frequencies satisfying

$$\left|\frac{A_0 + D_0}{2}\right| \le 1, \tag{10}$$

while frequencies that violate this condition lie within the stopband.[71]

In the trivial phase, the electromagnetic field within the stopband exhibits evanescent behavior, with amplitude decaying exponentially along the circuit, thereby effectively suppressing signal propagation.

The admittance spectral properties of the Laplacian matrix $\boldsymbol{L}$ motivate a detailed investigation of the frequency-dependent input impedance response of the entire system. Following the two-point resistance theorem,[73] with the excitation applied at port 1, the system's input impedance can be expressed in terms of the $\boldsymbol{L}$'s eigenvalues λ_i and its associated left and right eigenvectors, $\boldsymbol{\varphi}_i^{\mathrm{T}} = [\varphi_{i1}, \ldots, \varphi_{i2N}]$ and $\boldsymbol{\psi}_i = [\psi_{i1}, \ldots, \psi_{i2N}]^{\mathrm{T}}$, as

$$Z_{\mathrm{in}} = \sum_{i=1}^{2N} \frac{\psi_{i1}\varphi_{i1}}{\lambda_i\boldsymbol{\varphi}_i^{\mathrm{T}}\boldsymbol{\psi}_i}\,, \tag{11}$$

where $\boldsymbol{\varphi}_i$ and $\boldsymbol{\psi}_j$ are orthogonal if and only if $i \neq j$. This formulation holds for circuit networks of arbitrary dimensionality. However, in the one-dimensional circuit investigated in this study, the input impedance Z_{in} can be alternatively characterized by the elements of the system's total transmission matrix $\boldsymbol{T}_N$ as $Z_{\mathrm{in}} = A_N/C_N$ (see the SM). Since the entire circuit can be regarded as a cascade of two-port networks along the z-axis [Figs. 1(b) and 1(c)], when the system includes N unit cells, its overall transmission matrix $\boldsymbol{T}_N$ is obtained by successively multiplying the transmission matrices of each individual segment.

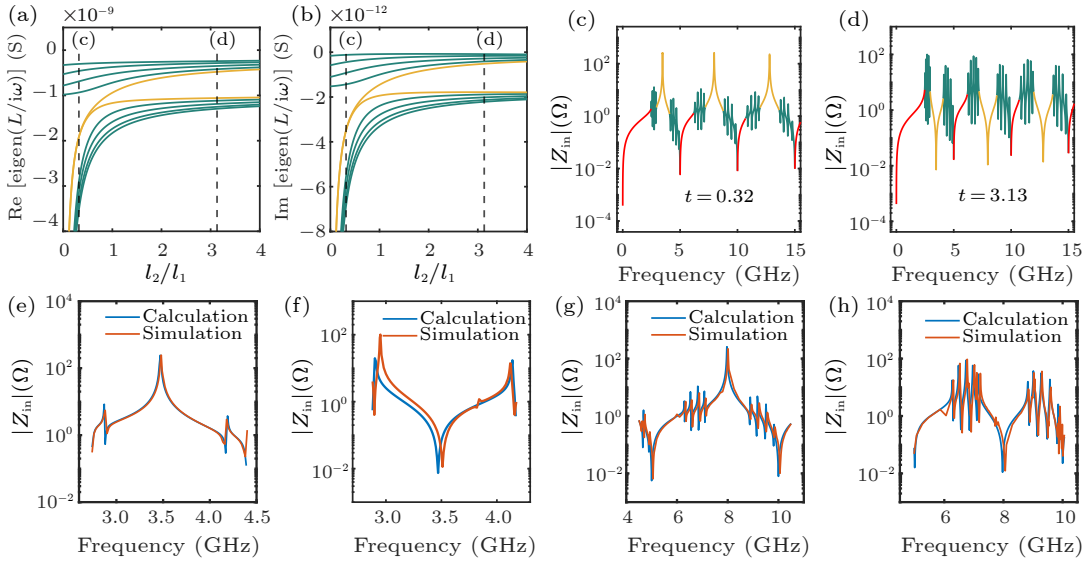

Fig. 2. Numerical results for the admittance and impedance responses of the one-dimensional, five-unit-cell parallel-plate transmission line topolectrical circuit. (a) and (b) Real and imaginary components of the frequency-normalized Laplacian eigenvalue spectrum. (c) and (d) Frequency-dependent input impedance under topologically nontrivial and trivial phases, calculated using the transmission matrix method in MATLAB. Green lines indicate the passbands determined under periodic boundary conditions (PBC) in the limit $N \to \infty$. Red and yellow lines indicate stopbands, with yellow specifically marking the inter-passband gaps, i.e., the frequency intervals between adjacent passbands within each periodic spectral segment, which only exhibit TBR in the nontrivial configuration (c). (e)–(h) Comparison between high-frequency electromagnetic simulations performed using Ansys HFSS and numerical results obtained from the transmission matrix corresponding to (a) and (b). As shown in (c) and (d), the input impedance exhibits periodic variation. Panels (e) and (f) highlight the topological boundary resonance with trivial-phase cutoff in the 0–5 GHz range in both the nontrivial and trivial configurations, while panels (g) and (h) present the corresponding features in the 5–10 GHz range.

Our analysis focuses particularly on impedance responses within the stopbands, and more specifically within the frequency gaps between adjacent passbands. By setting the lengths of transmission line segments to $l_1 = 29.98\,\text{mm}$ and $l_2 = 9.58\,\text{mm}$, the topological phase parameter becomes $t = 0.32$, corresponding to the nontrivial phase indicated by the left vertical dashed line in Figs. 2(a) and 2(b). The trivial phase is realized by interchanging the two line lengths, i.e., $t = 0.32 \to 3.13$, as marked by the right dashed line in the same figures.

Under PBC, the inter-passband gaps in the 0–15 GHz frequency range are identified as 2.94–4.08 GHz, 7.20–8.76 GHz, and 11.97–13.63 GHz. These gaps are highlighted with yellow lines in Figs. 2(c) and 2(d), distinguishing them from the passbands (green) and the remaining stopbands (red).

Although the five-unit-cell system is subject to open boundary conditions, bulk-state impedance resonances are still observed within the PBC-defined passbands. More significantly, sharp impedance peaks emerge within the inter-passband gaps, precisely in the frequency ranges where PBC predicts suppression of wave propagation. Within these stopbands, bulk modes persist but make minimal contributions to Z_{in} in Eq. (11) because their eigenvalues λ_i lie far from zero (distant from the eigenresonance frequencies in the passbands), producing only a smooth baseline without sharp features. The pronounced resonance peaks observed within these stopbands therefore originate predominantly from localized topological boundary states, designated as TBRs.

Using Ansys HFSS, we simulate the system's frequency response over two intervals: 0–5 GHz [Figs. 2(e) and 2(f)] and 5–10 GHz [Figs. 2(g) and 2(h)]. The results show excellent agreement with those obtained from the transmission matrix method. Notably, the input impedance magnitude exhibits sharp resonant peaks of 242.83 Ω at 3.47 GHz and 254.67 Ω at 7.97 GHz, approximately two orders of magnitude higher than typical bulk-mode passband resonances.

The quality factors Q, calculated using the full width at half maximum method, are 188.75 and 279.95 for the two resonances, respectively, indicating outstanding frequency selectivity. Importantly, at these resonance frequencies, the diagonal elements of the Laplacian matrix $\boldsymbol{L}$ [Eq. (3)] satisfy $Y_s = 0$, signifying a resonant condition intrinsic to the network's topology. In the formation of TBR peaks, increasing the number of unit cells N drives the nontrivial boundary state eigenvalues ever closer to zero, thus raising the Q-factor toward saturation, while the smooth baseline from bulk-mode contributions and intrinsic material losses in the transmission line (characterized by R_0 and G_0) cap the achievable peak sharpness (see Fig. S5 and further details in the SM).

Furthermore, the absence of corresponding resonant peaks in the trivial phase confirms that these features arise exclusively from TBRs, reinforcing their nontrivial origin.

At last, we compare the normalized voltage amplitude distributions across the unit cell ports at the TBR res-

onance frequency (7.97 GHz) and a representative bulk-state resonance frequency within the passband (6.82 GHz), as shown in Fig. 3. At 7.97 GHz, the voltage amplitude exhibits clear exponential localization from the left boundary, decaying geometrically with a common ratio of $t = 0.32$, consistent with the topological boundary state predicted by the SSH model.

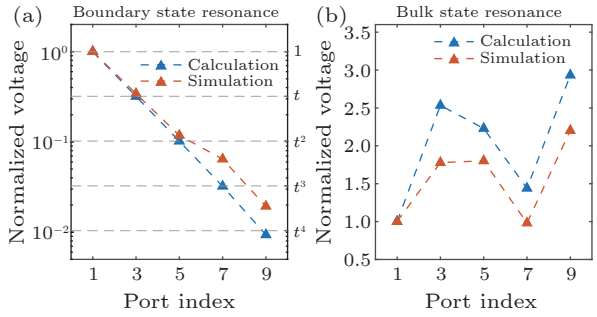

Fig. 3. Comparison of boundary and bulk state resonances based on the voltage distribution at odd-numbered ports, which correspond to A-sublattice sites within each SSH unit cell. (a) Voltage distribution at the TBR frequency 7.97 GHz, showing exponential localization from the left boundary with a geometric decay ratio of $t = 0.32$. (b) Voltage distribution at a representative passband resonance frequency 6.82 GHz, exhibiting spatial oscillations characteristic of bulk-state modes.

In contrast, the voltage distribution at 6.82 GHz, corresponding to a passband resonance, shows spatial oscillations characteristic of extended bulk states. The stark difference between exponential decay and oscillatory behavior highlights the topologically distinct nature of these two types of modes.

These results demonstrate that port-resolved voltage measurements offer an effective means of distinguishing topological boundary states from bulk states under non-trivial conditions in non-lumped topolectrical circuits.

The close correspondence between simulation and calculations, despite small deviations in Figs. 2 and 3, validates our approach. These minor discrepancies primarily stem from fringe field effect and the low loss approximation [Eq. (2)] that treats the transmission line's characteristic impedance Z_0 as a real constant rather than a frequency-dependent complex variable, as further detailed in the SM.

4. Conclusion. In this work, we propose and implement a non-lumped SSH topolectrical circuit based on a one-dimensional chain formed by alternating cascades of transmission line segments. We demonstrate that by tuning the lengths of the transmission lines, the system's topological properties can be precisely controlled, thereby determining the spectral positions of the TBR peaks. Numerical analyses reveal the existence of repeated, periodic, and high-Q TBRs in the frequency domain, with two representative cases successfully validated via full-wave electromagnetic simulations.

This proposal centers on the Laplacian matrix $\boldsymbol{L}$. By mapping $\boldsymbol{L}$ to the tight-binding Hamiltonian, it can be extended to generic topological models in various dimensions. Excitation may be applied at any port, allowing the input impedance to serve as a direct observable of the topological states. Our scheme can also be extended beyond lattice models to generate synthetic dimensions, similar to those realized in photonic waveguides,[55,74–76] but implemented using electrical transmission lines instead.

The proposed system enables flexible resonance tuning across a wide frequency range, from microwave to terahertz, that is difficult to achieve with conventional microwave resonators. Future work will explore its application across this broad spectrum.

Acknowledgmen.t X.Z. is supported by the National Natural Science Foundation of China (Grant No. 11874431) and the National Key R&D Program of China (Grant No. 2018YFA0306800). The calculations reported were performed on resources provided by the Guangdong Provincial Key Laboratory of Magnetoelectric Physics and Devices, No. 2022B1212010008.

References

[1] Lee C H, Imhof S, Berger C *et al.* 2018 *Commun. Phys.* 1 39
[2] Jia N, Clai Owens, Ariel Sommer *et al.* 2015 *Phys. Rev. X* **5** 021031
[3] Albert V V, Glazman L I, and Jiang L 2015 *Phys. Rev. Lett.* **114** 173902
[4] Goren T, Plekhanov K, Appas F, and Karyn Le Hur 2018 *Phys. Rev. B* **97** 041106
[5] Hadad Y, Jason C. Soric, Alexander B. Khanikaev, and Andrea Alù 2018 *Nat. Electron.* **1** 178
[6] Rafi-Ul-Islam S M, Siu Z B, Sahin H *et al.* 2022 *Phys. Rev. Res.* **4** 043108
[7] Pan N, Chen T, Ji T, Tong X, and Zhang X 2023 *Commun. Phys.* **6** 355
[8] Hohmann H, Hofmann T, Helbig T *et al.* 2023 *Phys. Rev. Res.* **5** L012041
[9] Su L, Jiang H, Wang Z *et al.* 2023 *Phys. Rev. B* **107** 184108
[10] Yuan H, Zhang W, Zhou Z *et al.* 2023 *Adv. Sci.* **10** 2301128
[11] Zhang H, Chen T, Li L *et al.* 2023 *Phys. Rev. B* **107** 085426
[12] Rafi-Ul-Islam S M, Siu Z B, Sahin H *et al.* 2024 *Phys. Rev. B* **109** 085430
[13] Pal A and Ghosh A K 2024 arXiv:2408.17152
[14] Zou D, Chen T, Meng H *et al.* 2024 *Sci. Bull.* **69** 2194
[15] Eisenberg Y, Barlas Y, and Prodan E 2019 *Phys. Rev. Appl.* **11** 044077
[16] Hofmann T, Helbig T, Lee C H *et al.* 2019 *Phys. Rev. Lett.* **122** 247702
[17] Wu J, Wang Z, Biao Y *et al.* 2022 *Nat. Electron.* **5** 635
[18] Yao J, Hao X, Song B *et al.* 2022 *Nano Futures* **6** 021001
[19] Yatsugi K, Yoshida T, Mizoguchi T *et al.* 2022 *Commun. Phys.* **5** 180
[20] Luo K, Yu R, and Weng H 2018 *Research* 2018
[21] Zhang X, Li G, Liu Y *et al.* 2021 *Commun. Phys.* **4** 47
[22] Lee C H, Sutrisno A, Hofmann T *et al.* 2020 *Nat. Commun.* **11** 4385
[23] Wang Y, Lang L J, Lee C H *et al.* 2019 *Nat. Commun.* **10** 1102
[24] Qi L, Wang G L, Liu S *et al.* 2020 *Phys. Rev. A* **102** 022404
[25] Stegmaier A, Imhof S, Helbig T *et al.* 2021 *Phys. Rev. Lett.* **126** 215302
[26] Liu S, Shao R, Ma S *et al.* 2021 *Research* **2021** 5608038
[27] Liu Y, Cao W, Chen W *et al.* 2022 *Sci. Rep.* **12** 13410

[28] Rafi-Ul-Islam SM, Siu Z B, Sahin H *et al.* 2022 *Phys. Rev. B* **106** 075158
[29] Hu W, Ruan B, Lin W *et al.* 2024 *Commun. Phys.* **7** 204
[30] Zhang X, Zhang B, Zhao W, and Lee C H 2024 *SciPost Phys.* **16** 002
[31] Tymchenko M and Alù A 2016 Circuit-based magnetless oquet topological insulator *2016 10th International Congress on Advanced Electromagnetic Materials in Microwaves and Optics (METAMATERIALS)* p 373
[32] Ezawa M 2018 *Phys. Rev. B* **98** 201402
[33] Imhof S, Berger C, Bayer F *et al.* 2018 *Nat. Phys.* **14** 925
[34] Liu S, Gao W, zhang Q *et al.* 2019 *Research* **2019**, 8609875
[35] Olekhno N A, Kretov E I, Stepanenko A A *et al.* 2020 *Nat. Commun.* **11** 1436
[36] Song L, Yang H, Cao Y, and Yan P 2020 *Nano Lett.* **20** 7566
[37] Zhang Z Q, Wu B L, Song J, and Jiang H 2019 *Phys. Rev. B* **100** 184202
[38] Zhang W, Zou D, Pei Q *et al.* 2021 *Phys. Rev. Lett.* **126** 146802
[39] Zhu W, Long Y, Chen H, and Ren J 2019 *Phys. Rev. B* **99** 115410
[40] Zou D, Chen T, He W *et al.* 2021 *Nat. Commun.* **12** 7201
[41] Lu Y, Jia N, Su L *et al.* 2019 *Phys. Rev. B* **99** 020302
[42] Wang Y, Price H M, Zhang B, and Chong Y D 2020 *Nat. Commun.* **11** 2356
[43] Guo S, Huang J, Huang R *et al.* 2023 *J. Phys. D: Appl. Phys.* **56** 505305
[44] Xiao M, Zhang Z, and Chan C T 2014 *Phys. Rev. X* **4** 021017
[45] Ota Y, Katsumi R, Watanabe K *et al.* 2018 *Commun. Phys.* **1** 86
[46] Henriques J C G, Rappoport T G, Bludov Y V *et al.* 2020 *Phys. Rev. A* **101** 043811
[47] Klauck F, Heinrich M, and Szameit A 2021 *Photonics Res.* **9** A1
[48] Khanikaev A B, Mousavi S H, Tse W K *et al.* 2013 *Nat. Mater.* **12** 233
[49] Lin J Y, Hu N C, Chen Y J, Lee C H, and Zhang X 2017 *Phys. Rev. B* **96** 075438
[50] Shalaev M I, Walasik W, Tsukernik A *et al.* 2019 *Nat. Nanotechnol.* **14** 31
[51] Xie B Y, Su G X, Wang H F *et al.* 2019 *Phys. Rev. Lett.* **122** 233903
[52] Zeuner J M, Rechtsman M C, Plotnik Y *et al.* 2015 *Phys. Rev. Lett.* **115** 040402
[53] Blanco-Redondo A, Andonegui I, Collins M J *et al.* 2016 *Phys. Rev. Lett.* **116** 163901
[54] Blanco-Redondo A, Bell B, Oren D *et al.* 2018 *Science* **362** 568
[55] Zhang X, Chen Y, Wang Y *et al.* 2019 *Phys. Rev. B* **100** 041110
[56] Efremidis N K 2021 *Phys. Rev. A* **104** 053531
[57] Yang Y, Zuo Z, and Cao D 2021 *Phys. Rev. A* **104** 043710
[58] Rechtsman M C, Zeuner J M, Plotnik Y *et al.* 2013 *Nature* **496** 196
[59] Chen W J, Jiang S J, Chen X D *et al.* 2014 *Nat. Commun.* **5** 5782
[60] Zhang Z Q and Sheng P 1994 *Phys. Rev. B* **49** 83
[61] Zhang Z Q, Wong C C, Fung K K *et al.* 1998 *Phys. Rev. Lett.* **81** 5540
[62] Hu W, Pillay J C, Wu K *et al.* 2015 *Phys. Rev. X* **5** 011012
[63] Jiang T, Xiao M, Chen W J *et al.* 2019 *Nat. Commun.* **10** 434
[64] Guo Q, Jiang T, Zhang R Y *et al.* 2021 *Nature* **594** 195
[65] Whittaker D and Ellis R 2021 arXiv:2102.03641
[66] Whittaker D, McCarthy M M, and Duan Q 2023 arXiv:2311.11040
[67] Su W P, Schrieffer J R, and Heeger A J 1979 *Phys. Rev. Lett.* **42** 1698
[68] Levy R, Snyder R, and Matthaei G 2002 *IEEE Trans. Microwave Theory Tech.* **50** 783
[69] Capmany J, Ortega B, and Pastor D 2006 *J. Lightwave Technol.* **24** 201
[70] Huss S 1995 A mathematical and lumped-element model for multiple cascaded lossy transmission lines with arbitrary impedances and discontinuities *Proceedings of ISCAS '95-International Symposium on Circuits and Systems* **3** p 1844
[71] Pozar D M 2012 *Microwave Engineering* 4th ed (Hoboken, New Jersey: John Wiley & Sons)
[72] Ludwig R and Bretchko P 2000 *RF Circuit Design: Theory and Applications* (Upper Saddle River, New Jersey: Prentice-Hall)
[73] Cernanová V, Brenkus J, and Stopjaková V 2014 *Journal of Electrical Engineering* **65** 283
[74] Lustig E, Weimann S, Plotnik Y *et al.* 2019 *Nature* **567** 356
[75] Yuan L, Lin Q, Xiao M, and Fan S 2018 *Optica* **5** 1396
[76] Ozawa T, Price H M, Amo A *et al.* 2019 *Rev. Mod. Phys.* **91** 015006